Supplemental

Unexpected high binding energy of CO_2 on $CH_3NH_3PbI_3$ lead-halide organic-inorganic perovskites via bicarbonate formation

M. T. Nayakasinghe,[a] Y. Han,[a] N. Sivapragasam,[a] D. Kilin, [a]* and U. Burghaus [a]*

[a]Department of Chemistry and Biochemistry,
North Dakota State University (NDSU), Fargo, ND 58108, USA

* Correspondence authors:

FAX 701.231.8831

uwe.burghaus@ndsu.edu   www.uweburghaus.us

dmitri.kilin@ndsu.edu   https://www.ndsu.edu/chemistry/

A list of abbreviations is at the end of this document.

Brief literature survey - carbon dioxide

Reviews and comprehensive papers about CO_2 surface chemistry can be found in ref.[1-5]

Carbon dioxide chemistry has attracted increased interest for many years, motivated by environmental concerns and the utilization of CO_2 as a feedstock for the chemical industry.[1-4, 6] The numerous systems studied in surface science may roughly be described as those that clearly form carbonates (oxide surfaces such as CaO, MgO) and those that only physisorb CO_2 (e.g. Cu, Pt) at ultra-high vacuum (UHV) conditions.[3] Also, a few surfaces have been studied where CO_2 may dissociate (e.g. Nickel surfaces). Thermal desorption spectroscopy (TDS) desorption temperatures of physisorbed CO_2 are typically below 200 K, carbonate decomposition is seen at about 600 K. Detailed discussions of the (even for small molecules complex) gas phase electronic structure for CO_2 can be found in various sources.[1, 2, 7] CO_2 adsorption has apparently not been studied on $CH_3NH_3PbI_3$ at UHV. The closest systems considered in the literature we are aware of may be perovskite oxides such as $LaMnO_3$ or $BaTiO_3$.[8, 9] Although the chemistry on oxide surfaces will be quite different than for $CH_3NH_3PbI_3$, at least these materials have similar crystal structures. Further literature discussion is also part of the main draft.

Materials

The $CH_3NH_3PbI_3$ precursor solution (1.37 g/mL in 40% DMF - dimethylformamide) was purchased from Sigma Aldrich. The indium doped tin oxide glass (ITO) substrates were also from Sigma Aldrich. For the UHV experiments, the research grade gases (from Praxair) were dosed by backfilling the vacuum chambers via a precision leak valve with exposures, χ, given in Langmuir (1 L = 1 × 10^{-6} Torr x 1 s). Numerous freeze-pump-thaw-cycles were applied to degas the liquid attached by a metal-glass flange to a leak valve.

A typical $CH_3NH_3PbI_3$ crystal structure consists of an inorganic (PbI_3) and organic methylammonium (CH_3NH_3) sublattice. The PbI_3 lattice is octahedral with Pb in the center and iodine at the six corners (vertices). The methylammonium ions occupy the interstitials (cavities) between successive octahedra.

Experimental procedures

Ambient pressure as well as ultra-high vacuum (UHV) based experimental techniques were used; the former mainly for the purpose to connect to prior engineering works.

Experimental set up and procedures - ultra-high vacuum experiments

For convenience, the experiments were conducted in two different ultra-high vacuum (UHV) chambers. Both systems are equipped with mass spectrometers for thermal desorption spectroscopy (TDS) as well as the common surface science tools.[10] TDS, a temperature ramping method, is used to characterize the adsorption/desorption kinetics and thermal stability of the samples. One UHV system has CMA (cylindrical mirror analyzer) based Auger electron spectroscopy (AES), the other one houses a retarding field AES and LEED (low energy electron diffraction) setup.

TDS The nanoscience community is diverse; many different measuring techniques are common, which sometimes causes confusion. However, the UHV experimental techniques used in our study are described in common textbooks of surface science. In addition, details about the measuring techniques we use and our set-up also can be found in the supplemental to ref.[11] (molecular beam scattering details) and ref.[12] (thermal desorption spectroscopy). (We would like to avoid to rewrite these supplementals here.)

The lowest adsorption temperature accessible amounts to ~90 K, the greatest temperature used was 850 K. The heating rate amounts to $\beta = 1.6$ K/s.

Experimental set up – ambient pressure experiments

UV-vis and surface thickness experiments were conducted at ambient pressure. In addition, XRD (X-ray diffraction), EDX (energy-dispersive X-ray spectroscopy), and SEM (Scanning Electron Microscope) data were collected to characterize the samples prior to the UHV kinetic experiments.

SEM/EDX. For SEM, a JEOL's JSM-6010LA with an integrated energy dispersive spectroscopy (EDS or EDX) unit was used for sample imaging.

UV-vis. Different UV-vis spectrometers were used throughout the project (Carry 5000, Carry 50Bio from Varian, see data below). The spectra shown below were collected with a Varian carry 5000. It also enables the analysis in both transmittance and diffuse reflectance modes.

Surface profiler. A surface profiler (P11 from Tencor) was used to estimate the thickness of selected perovskite film samples.

Spin coater. A commercial spin coater (P6700 from Specialty coating system Inc.) as well as a home built one was used, both under N_2 flow, to spin coat the perovskite film.

XRD. X-ray diffraction scans were recorded on a Bruker D8 Discover system utilizing a Copper X-ray source followed by a Primary Gobel Mirror and on through a 0.5mm collimator. The Detector is a Vantec 500 Area Detector that captures 27 degrees of the 2theta range. The scans were collected utilizing 4 frames at 120 seconds capture time for each frame. Initial scans were started at Omega (Theta) 7.5 degrees and 2theta at 15 degrees. Scans were taken at 15, 30, 45, and 60 degrees 2theta cover a range from 1.5 degrees to 73.5 degrees. Phi was 90 degrees and Chi was 90 degrees. Scan axis were coupled in the Step mode. Frame width was 15 degrees. The sample was scanned in the X axis in a 1mm amplitude during the scans. Data was integrated utilizing Discover EVA software from Bruker and then translated to Raw data through Jade Data Analysis Software.

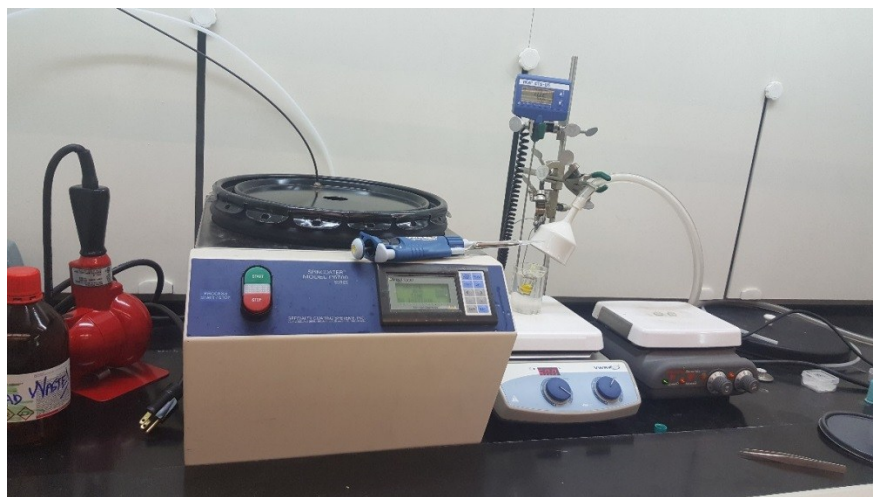**Sample synthesis set-up (NDSU surface science group/NDSU research Park)**

Fig. S1: Benchtop set-up for ambient pressure synthesis of the perovskites. The process used here is commonly applied in a number of studies, see e.g. ref.[13]

Fig. S1 shows the experimental set up for the perovskite synthesis. The spin coater is programmed to run at 4000 rpm for 30 seconds. Nitrogen is continuously flowed through the top section of the spin coater. One hotplate is set at 70 ºC to maintain an oil bath at 70ºC. The precursor solution (methyl ammonia triiodo pulmbate) is kept in that oil bath under nitrogen atmosphere (nitrogen blanket created with Buchner funnel) and maintained at 70 ºC. Another

hotplate is set to 100 ºC for annealing the films. A glove box large enough to fit the spin coater was not available.

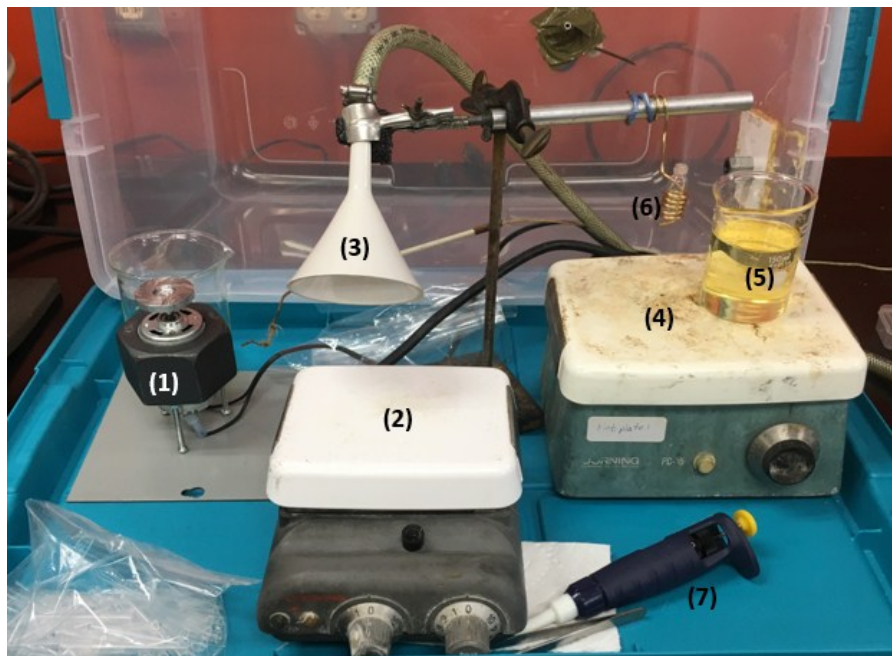**Sample synthesis set-up (NDSU/chemistry department)**

Fig. S2: Benchtop set-up for ambient pressure synthesis of the perovskites. 1) Homemade spin coater (~3000 rpm) using a cheap DC motor in a mounting bracket; 2) Hot plate for sample heating after the synthesis; 3) Nitrogen blanket; 4) Hot plate for the precursor solution heating; 5) Thermostat oil bath (MPO-200); 6) Precursor solution holder; 7) Micropipette

A 2nd setup was used to synthesis samples, see Fig. S2. This setup was in close proximity of the vacuum chambers and UV-vis reducing sample transfer time through air.

Perovskite synthesis summary

We used an ambient pressure wet chemistry procedure commonly described in the literature.[13, 14] Briefly, the as received substrates were initially cleaned with water, acetone, and ethanol. 60 μL of $CH_3NH_3PbI_3$ precursor solution, maintained at 350 K (70 ºC), was spin coated at 4000 rpm (or 3300 rpm) for 30 seconds. The spin coated samples were annealed on a hot plate at ~380 K (100 ºC) for 10 minutes.

This synthesis was carried out in a flow of dry N_2. The as prepared samples were immediately placed into a N_2 filled container. Samples transferred to UHV were degassed in UHV at temperatures up to 380 K. Higher degassing temperatures destroy the samples; ion sputtering for cleaning cannot be used on these thin film samples. Thus, sample cleaning is limited, but the UHV environment prevents accidental adsorption of contaminations. Data collected from numerous different samples are shown since these samples decompose or change irreversibly during the course of our experiments.

Perovskite synthesis step by step

We copied a procedure described before in the literature:[13]

1. The glass slabs were cut into 10x10x0.3 mm pieces to fit into the sample holder

2. The glass slabs were then washed with distilled water, acetone, and ethanol to remove contaminants

3. The washed glass slabs were used to synthesize perovskite films as described below:

4. A 60 µl precursor solution was transferred onto the FTO glass slab kept on the spin coater. The sample was then spin coated at 4000 rpm for 30 seconds under nitrogen atmosphere (Fig. S1 setup). (Or, at 3300 rpm using Fig. S2 set-up.) The spin coated film was then moved onto a hotplate and was annealed at 100 ºC for 15 minutes. The nitrogen blanket with Buchner funnel was maintained over the films during annealing. The annealed samples were transferred into nitrogen filled sample containers for further analysis.

5. The samples were usually characterized by UV-Visible spectroscopy before mounted in the UHV chamber for further analysis.

Details of the theoretical procedures

The adsorption of different gas molecules including CO_2 and H_2O were investigated theoretically. Binding energies (BE also denoted as E_d) were calculated by

$$BE = E_{slab} + E_{adsorbate} - E_{(slab+adsorbate)} \qquad (1)$$

where E_{slab}, $E_{adsorbate}$, and $E_{slab + adsorbate}$ represented the energy of the optimized structure of a pristine slab, isolated adsorbate molecule, and hybrid system with gas molecule adsorbed on the slab, respectively, all of which were reported from single point energy calculations based on optimized structures, with size of the simulation cell and basis set kept the same for all three calculations.

Density functional theory (DFT) calculations were performed on the basis of plane waves within the Vienna Ab initio Simulation Package (VASP).[15-18] We adopted the projected augmented wave (PAW)[19] potentials and the generalized gradient approximation (GGA)[20, 21] with Perdew-Burke-Ernzerhof (PBE)[21] exchange-correlation functional. The long-range inter-nuclear interactions were considered through the application of a semiempirical pairwise corrections i.e. DFT+D2. A plane wave energy cutoff was set as 500 eV. Throughout theoretical calculations, (4 × 4 × 4) and (4 × 4 × 1) Monkhorst−Pack k-point grids were used for the bulk crystal and slab models, respectively. To save numerical resources, we adopted spin restricted approaches for geometry optimization calculations. The spin-orbit coupling (SOC) effect has been found to play a significant role in electronic properties of $CH_3NH_3PbI_3$ perovskites.[22] To accurately describe electronic structures of atomic models, we then carried out single point energy calculation for optimized configurations with noncollinear spin approaches by taking into account SOC effects.[23-25]

The theoretical calculations focused on the orthorhombic phase of $CH_3NH_3PbI_3$ perovskite, which were less challenging than the tetragonal or cubic phase due to the presence of ordered $CH_3NH_3^+$ cations.[26] The initial lattice vectors and positions of ions for the bulk phase of orthorhombic $CH_3NH_3PbI_3$ were obtained from the XRD crystallographic data[27] and served as starting points for theoretical calculations. The atomic model of (001) surface was constructed based on relaxed bulk crystal. The (1x1x2) supercell, which was derived from the (1x1x1) unit cell of the bulk, consisted of four layers of PbI_2 atoms with a total of 96 atoms, giving a chemical formula of $(CH_3NH_3)_8Pb_8I_{24}$. A vacuum spacing layer of 15 Å was added normal to the (001)

surface to minimize any spurious interaction. Overall size of the rectangular simulation cell reads (a = 8.706 Å, b=12.395 Å, and c=31.858 Å), with periodic boundary conditions imposed in each direction. We also constructed a vacancy structure on the basis of (001) surface model by removing a surface $CH_3NH_3^+$ cation and I^- anion in the second PbI_2 layer, giving a chemical formula of $(CH_3NH_3)_7Pb_8I_{23}$. In geometry optimization calculations, all atoms were allowed to relax for the bulk, while all atoms except the bottom Pb layer were allowed to relax for the slab models.

Additional data – sample characterization / standard sample characterization

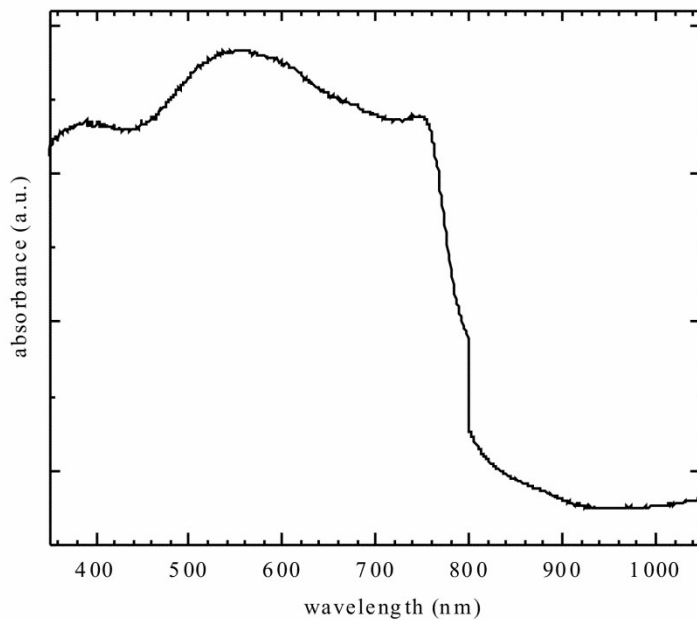**Optical properties – UV-vis**

Fig. S3: UV-vis of a typical sample.

The most prominent UV-vis feature is a shoulder at 800 nm, present for all samples and in agreement with prior works.[28, 29] The appearance of this absorption is an indication for the successful chemical transformation of the liquid precursor solution into the solid perovskite film. (the step at 800 nm is caused by switching lamps of the UV-vis).
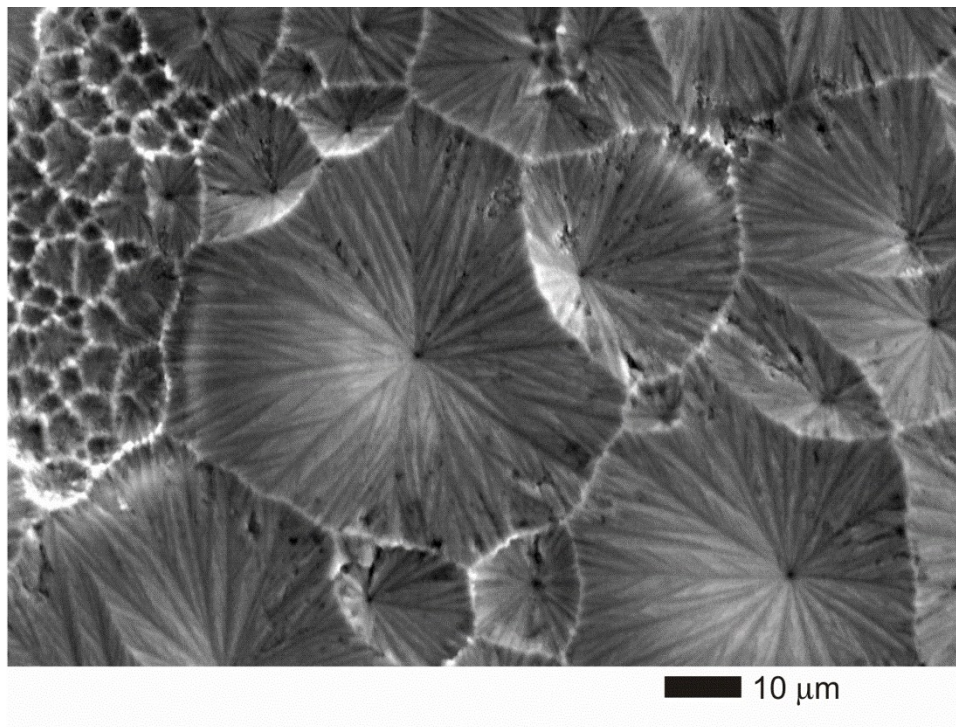
Sample imaging SEM (scanning electron microscope)

Fig. S4: SEM of a typical sample.

Fig. S4 depicts a SEM micrograph of a typical sample. Structurally very similar images can be found in ref.[13] which again verifies that our sample preparation was successful. Our larges structures have a diameter of about 60 μm.
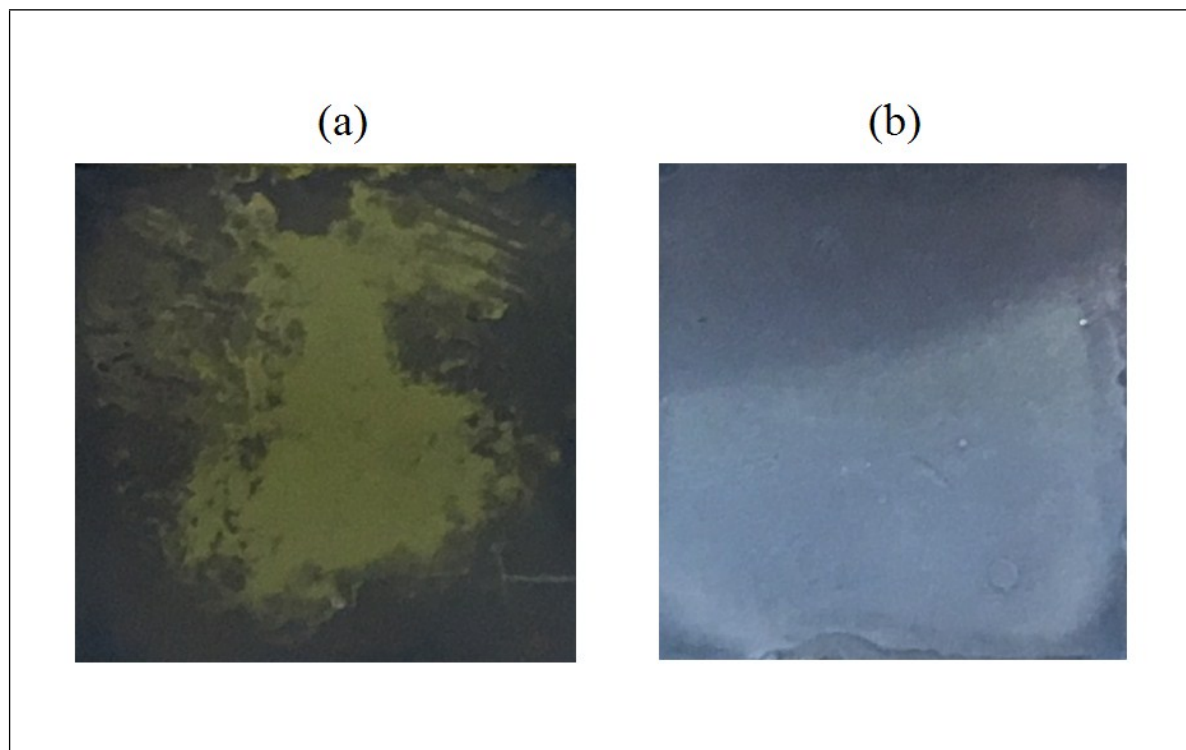
Sample imaging optical camera

Fig. S5: A) Photo of a decomposed (over heated, 200ºC) perovskite sample (PbI$_2$) and
B) a good sample. Photos made using a digital camera. (Using set-up of Fig. S2)

For images recorded with a digital camera, see Fig. S5. Good samples have a brown or gray appearance (depending on film thickness) whereas decomposed samples are yellow.

Film thickness measurement

Y axis	Thickness/nm
1000	759.9
1200	630.6
1400	631.8
1600	787.0
1800	608.8
2000	643.7
2200	647.8
2400	530.1
2600	644.9
2800	593.8
Sum	**6478.4**
Ave	**647.8**
SD	**75.1**

Tab. S1: Results of film thickness measurement of one sample synthesized with the setup in Fig. S1.

Using a surface profiler the film thickness was determined (Tab. S1) for one of the samples and did amount to (648±75) nm, literature values (330 nm, ref.[30]; 300 nm, ref.[28]) are within the same order of magnitude. Differences in details of the spin coating process and the amount of solution used can cause variations in film thickness. Surface profiling is a destructive process, i.e., the samples cannot be used for any further experiments.
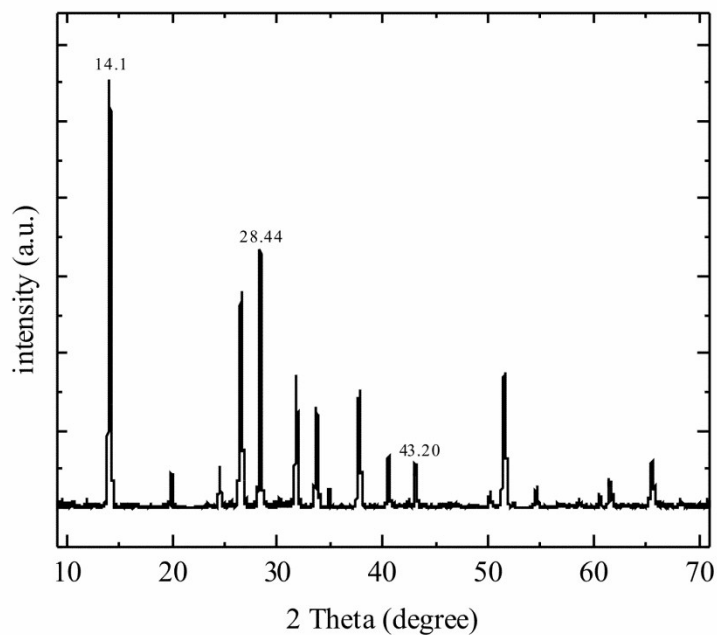
Sample crystallinity

Fig. S6: XRD (X-ray diffraction) scan.

A XRD scan is depicted in Fig. S6. Our sample had diffraction peaks at 14.12º, 28.44º, 43.23º representing the 110, 220, 330 planes of the orthorhombic crystal structure of the $CH_3NH_3PbI_3$ perovskite at room temperature.[31] The remaining peaks originate from the substrate. The fact that diffraction peaks are detected at all is consistent with a polycrystalline structure of the sample. The crystallites also are apparent in SEM images. Temperature dependent changes of the crystal are reported in the literature.[32]
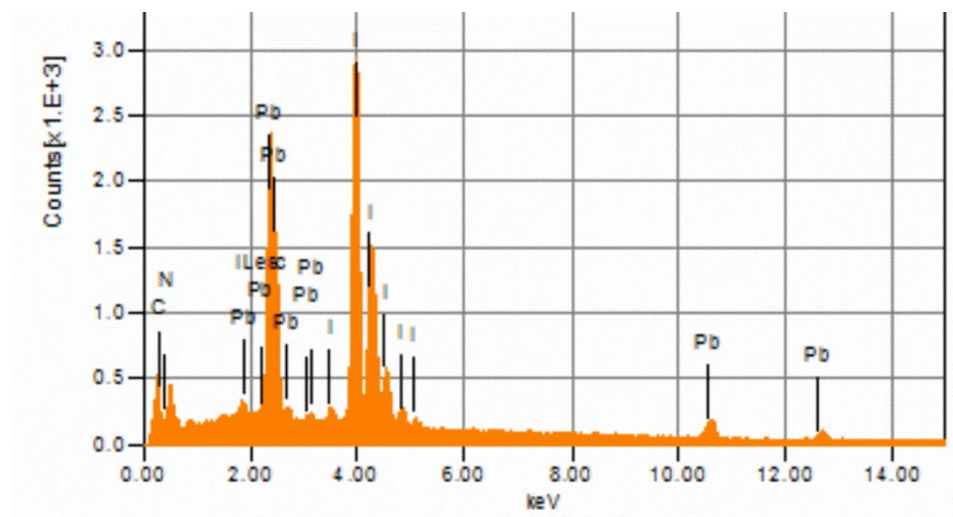
Sample's chemical composition - EDX

Fig. S7: EDX (energy dispersive spectroscopy).

The chemical composition of one sample was determined with EDX (Fig. S7). Additionally, throughout the UHV experiments frequent Auger scans were collected, see below. According to EDX, C, Pb, I, N are present, as expected.

Tab. S2 summarizes the composition, as obtained from the EDX software package. Qualitatively consistent with the AES data (see below), the samples have too much carbon being just stoichiometric. For example, the molar EDX C to I ratio amounts to 0.8, whereas the stoichiometry of $CH_3NH_3PbI_3$ would suggest a ratio of 1 to 3. In contrast, EDX detects a 1 to 2.3 ratio for Pb and I which is reasonable close to what it should be stoichiometrically (namely 1:3), similar to literature reports, see ref.[33] Thus, the samples are carbon contaminated due to ambient exposure. That cannot entirely be avoided and is typical for solution-based ambient pressure sample synthesis which is the most common synthesis procedure found in many publications.

	ms%	mol%
C	6.55	46.84
N	0.04	0.25
I	53.96	36.55
Pb	39.45	16.37
Total	100.00	100.00

Tab. S2: Elemental analysis based on the EDX scan given as Fig 5. The analysis is done by the SEM software.

Result of an EDX experiment. ms% denotes atomic mass to molecular weight (in percent) ratio. E.g. for carbon 12/molecular weight * 100.

Measured molar C to I ratio is C=46.84 to I=36.55 or 1 to 0.78.
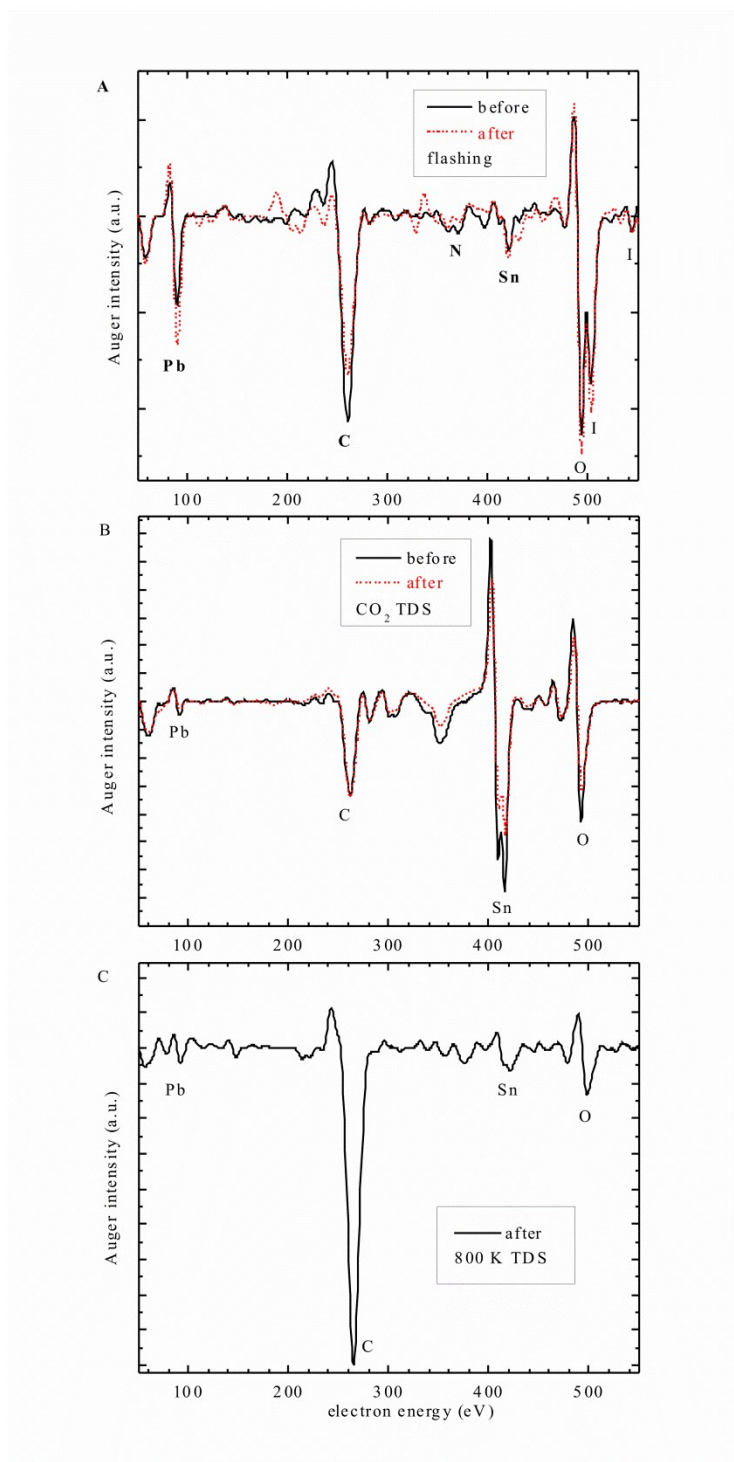
Sample's chemical composition - Auger

Fig. S8: AES spectra (Auger electron spectroscopy). AES scans of a perovskite sample transferred to UHV. Solid lines **A)** before and **C)** after a TDS temperature ramp of 200-800 K in UHV. **B)** bare ITO substrate. (Dashed line in A is collected after a quick 380 K UHV flash; dashed line in B after CO_2 TDS.)

16

The solid line in Fig. S8A depicts an AES spectrum of a perovskite sample synthesized at ambient and immediately transferred to the UHV chamber (within ~45 min). The AES scans show Pb, C, N, Sn, O, and I peaks. Most but not all of these originate from the $CH_3NH_3PbI_3$ perovskite.

The penetration depth of the AES electrons is larger than the perovskite film thickness, i.e., the signals also originates in part from the ITO substrate. Therefore, a Tin peak is detected in AES (at 420 eV, Fig. S8A), however, no Si peak (would be at 90 eV) from the glass on which the ITO layer is deposited. Thus, it becomes evident that AES does sample the perovskite layer, ITO (indium doped tin oxide) coatings, adsorbates, and interstitial impurities. AES scans of the bare substrate (Fig. S8B) show an even larger Tin (Sn) peak which is suppressed for the samples due to screening effects by the perovskite film. (The indium as a dopant of ITO is below the detection limit of the AES system.)

Interestingly, the relative O-AES peak intensity (e.g. O-to-Sn ratio) of the substrate alone (Fig. S8B) is smaller than for the perovskite film (Fig. S8A). Therefore, only part of the O-AES signal originates from the ITO substrate, but part of it must be from oxygen containing adsorbates rather than the ITO/glass layer. The most likely oxygen containing impurity is water adsorbed from the ambient, as we can see indeed more quantitatively in the TDS data (main draft).

Consistent with the EDX data, the carbon AES peak (Fig. S8A) is too large for originating only from the perovskite, indicative of impurity take-up during the ambient pressure synthesis.

The dashed line in Fig. S8A shows an AES scan after UHV flashing the sample to 380 K. The C AES intensity decreases and the Pb peak increases. Thus, the UHV flash to 380 K initially cleaned the sample. Carbon containing impurities partially desorbed and/or diffused deeper into the bulk of the sample.

After the AES characterization of a typical "pristine" sample, the sample temperature was once ramped up to 720 K and then to 850 K in UHV. Again an AES scan was collected, see Fig. S8C. The graph in Fig. S8C compares scans taken before (solid line same as in Fig. S8A) and after (dashed line) the 850 K ramp. The Sn peak is not changing, i.e., the substrate is not directly affected, as expected. The Pb peak intensity distinctly decreased, the I AES signal is not detectable, consistent with the desorption of the perovskite film. Note the double peak at ~500

eV from oxygen and iodine for an intact perovskite sample which converts into a single peak (oxygen) when the perovskite desorbs. When the perovskite decomposes (rather than desorbs), proposedly to adsorbed PbI_2,[14, 34] then an Iodine I-AES peak is present. That is the case for temperature ramps not exceeding 600 K.

Part of the adsorbed water desorbed since the O-peak intensity decreased after the high temperature ramp (Fig. S8C). Unfortunately, the carbon peak now dominates the AES scan. Thus, further flashing does not clean the sample further, but rather decomposes it. The C AES peak increases since the perovskite film mostly desorbs, exposing now the ITO and glass substrates which are carbon contaminated. The C signal was originally smaller due to screening of the carbon/ITO by the perovskite. The AES data are consistent with the EDX discussed earlier. The samples are carbon contaminated which is typical for solution-based ambient pressure sample synthesis. That synthesis is, however, the most common synthesis procedure found in many publications. The solution-based synthesis makes the material interesting for many applications.

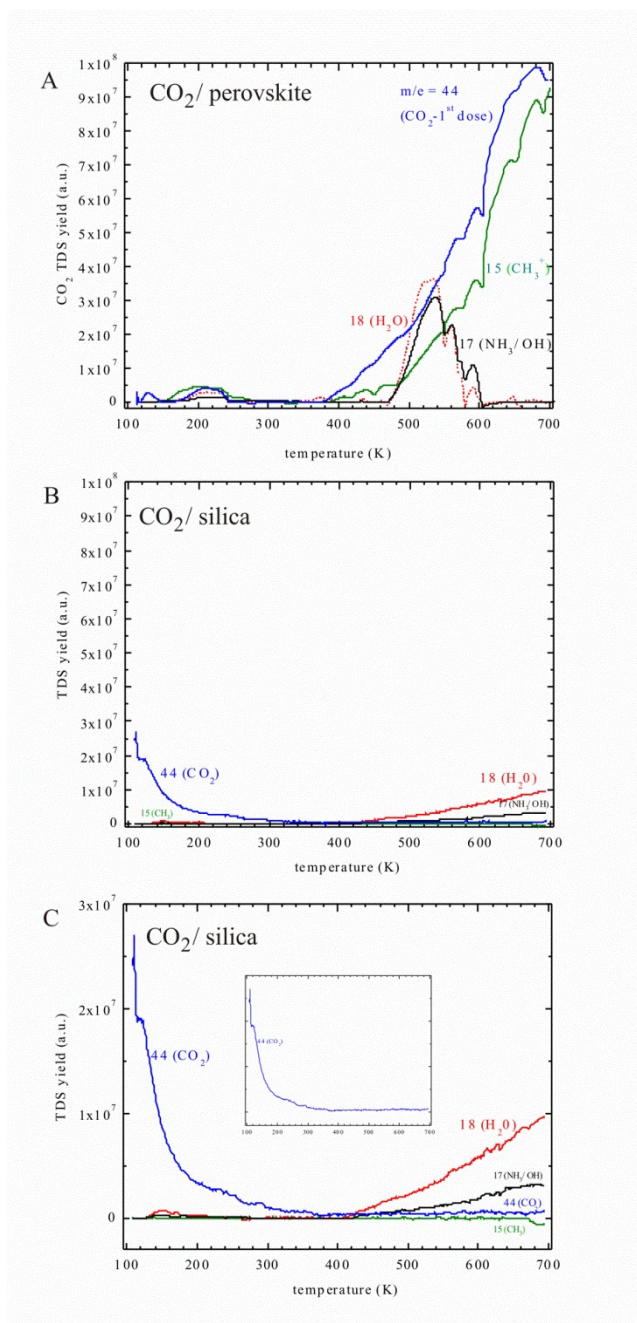**Additional TDS data – CO$_2$ blind experiments**

Fig. S9: Blind experiment. A) CO$_2$ adsorption experiment, multi-mass TDS (20 L, large exposure) **B & C)** CO$_2$ blind experiments with a silica sample mounted on the same sample holder. Multi-mass TDS experiment. (For all experiments 20 L CO$_2$ were dosed at low temperature.) Panels B and C show the same data on different scales. Panels A and B are plotted using the same scales.

Does CO_2 desorb/adsorb on the sample and/or somewhere else in the UHV chamber such as the sample holder? Ruling out sample holder effects, a silica samples was mounted on the same sample holder in the same UHV chamber with the same pump configuration. The CO_2 experiments were repeated with this silica sample. Clean and defect free silica does not adsorb CO_2 down to 95 K[35, 36] and can be considered a blind sample. Ideally any CO_2 desorption detected with the blind sample must come from the sample holder.

CO_2 As evident, CO_2 (blue lines) does not desorb from the blind sample above 400 K. (The scales in panel A and B are identical. Panel C shows an expanded intensity scale. The inset in C depicts only the CO_2 signal from silica.) Thus, the high temperature CO_2 desorption seen for the perovskite sample is indeed related to the perovskite sample and not the sample holder. The low temperature CO_2 desorption from silica can result from surface defects and/or functionalities such as adsorbed OH, H_2O, O_2, etc.

Water Traces for a few other masses are shown as well. Water desorption is seen, most likely indeed from the sample holder. (Silica can adsorb water molecularly; but in that case, the desorption temperatures would be lower.) However, the temperature profile of water/blind and water/perovskite are quite different as well as the intensity for the blind experiments are significantly lower (by a factor of 4). Therefore, one can conclude that some water desorption from the sample holder may affect the TDS data at high temperatures, but it does not dominate the results for the perovskite film.

Determination of the experimental kinetics parameters

Experimental binding energies, E_d, were determined from the TDS peak positions, T_{max}, (with uncertainty of ±0.5 kJ/mol) using the Redhead[37] equation.

For 1st order desorption this equation can approximately be written as

$E_d = RT_{max}[\ln(\frac{\nu T_{max}}{\beta}) - 3.64]$. (R is the gas constant, β the heating rate, pre-exponential is ν)

A typical pre-exponential for molecular adsorption is of $\nu = 1 \times 10^{13}$/s which we used to estimate. Similar data analysis can be done using a 2nd order Redhead[37] equation. 2nd order pre-exponentials are harder to find. A preexponential of 10^{21} cm^2/(mol sec) was invoked for H+H →H2 experiments, see refs.[38]

Further theoretical results

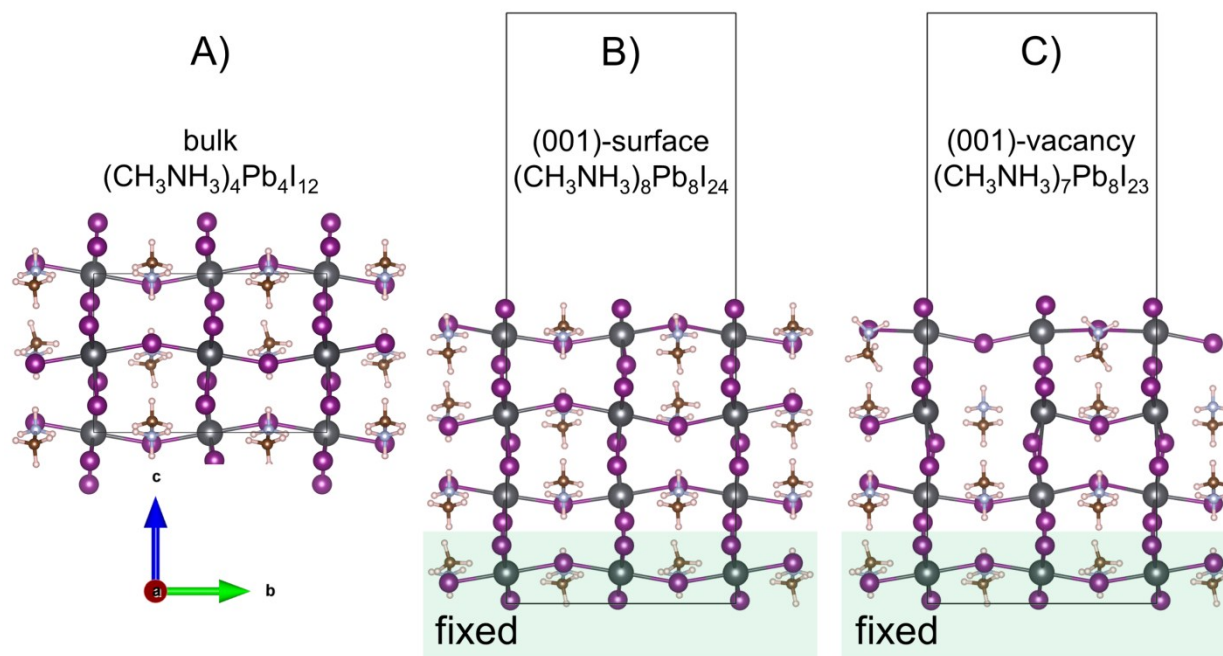**Fig. S10**: Atomic models of orthorhombic $CH_3NH_3PbI_3$ **A)** Crystal, **B)** slab representing the (001) surface, and **C)** defect structure. The unit cell of the perovskite crystal consists of 48 atoms, represented by the formula $(CH_3NH_3)_4Pb_4I_{12}$. The slab representing the (001) surface and vacancy models consist of 96 atoms as $(CH_3NH_3)_8Pb_8I_{24}$ and 87 atoms as $(CH_3NH_3)_7Pb_8I_{23}$, respectively. The box represents the simulation cell. ~~a~~ A vacuum spacing layer of 15 Å normal to the (001) surface is included for structures B) and C). The brown, pink, light blue, grey, purple, and red spheres denote C, H, N, Pb, I, and O, respectively. The green background in panels B) and C) indicates the bottom PbI_2 atom layer that is kept fixed during geometry optimization.
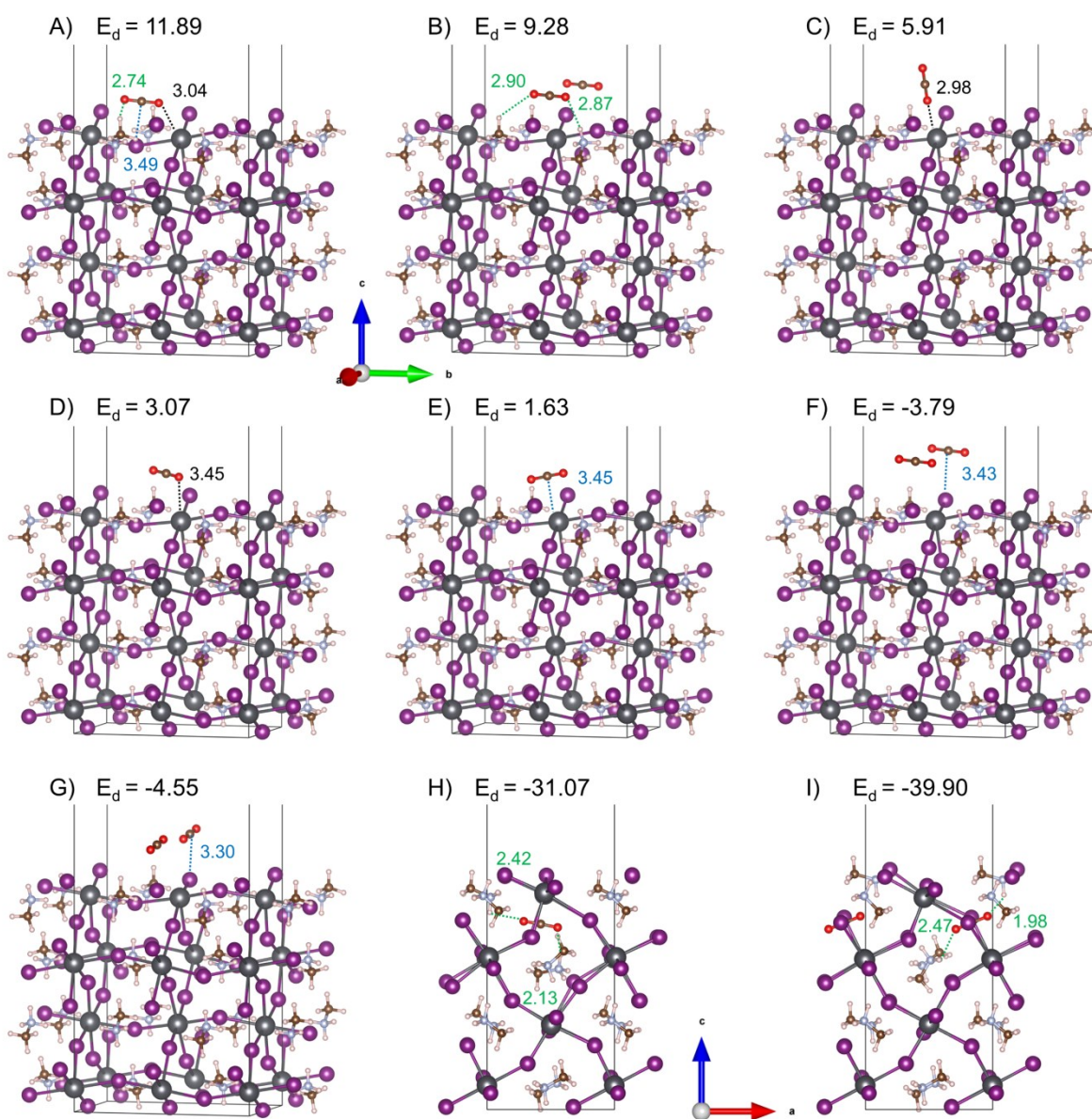
Fig. S11: Optimized configurations of the model structures adsorbed with CO_2. Configurations in panels **A-G)** correspond to CO_2 adsorbed on the surface, while those in panels **H-I)** correspond to CO_2 adsorbed inside the pore of the slab. The binding energies are in units of kJ/mol. The brown, pink, light blue, grey, purple, and red spheres represent C, H, N, Pb, I, and O, respectively. The box represents the simulation cell. The vacuum layers are not explicitly shown. Each cell contains one CO_2 molecule. Additional species seen in the figure are due to visualization under periodic boundary conditions. For selected atoms, the interatomic distances (in Ångstrom) are indicated.
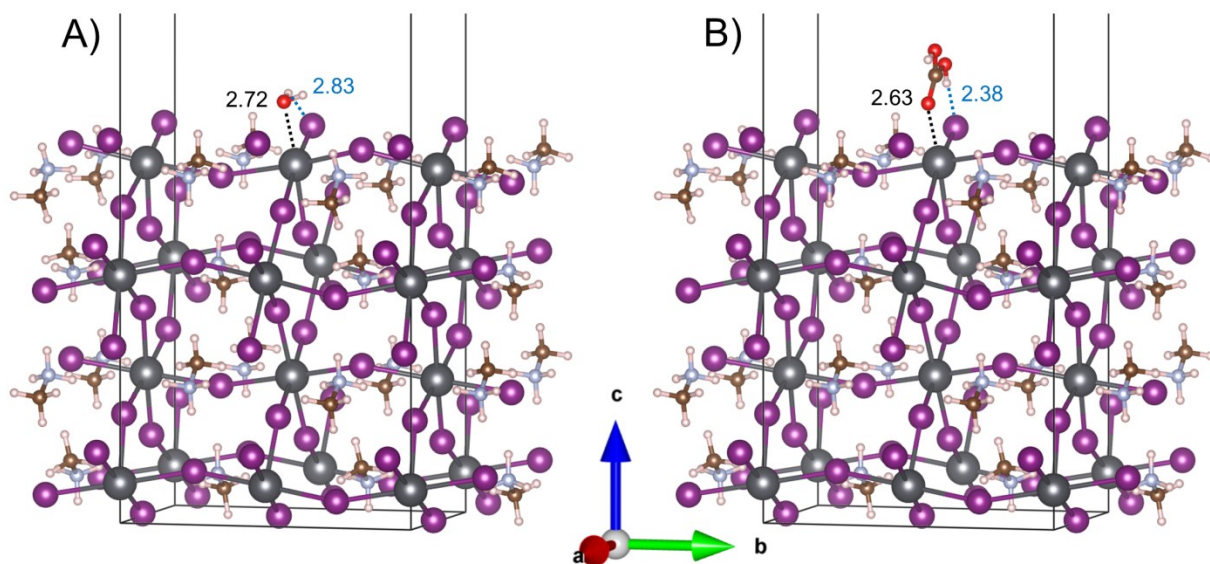
Fig. S12: Optimized configurations of the model structures adsorbed with **A)** H_2O and **B)** H_2CO_3. The brown, pink, light blue, grey, purple, and red spheres represent C, H, N, Pb, I, and O, respectively. The box represents the simulation cell. The vacuum layers are not shown. For selected atoms, the interatomic distances (in Ångstrom) are indicated.
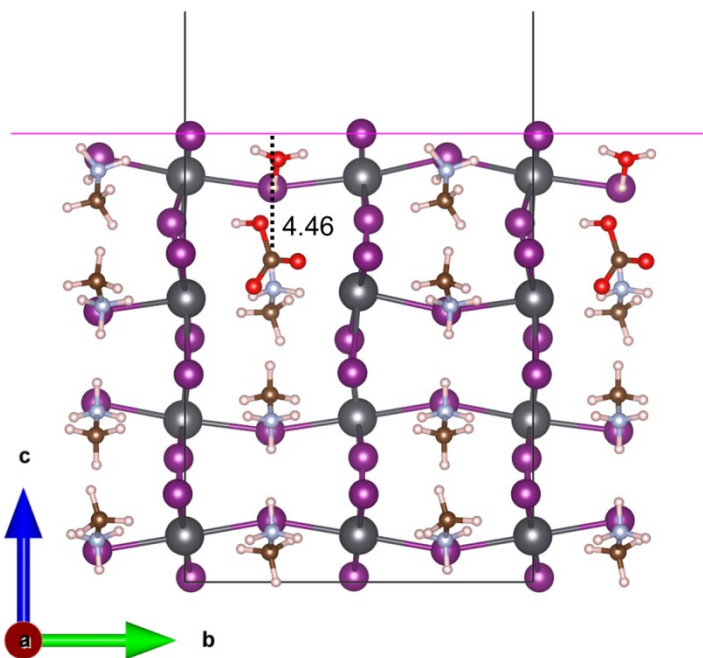
Reactive site just subsurface

Fig. S13: Active site is just subsurface. The defect structure with embedded H_3O^+ and HCO_3^-. The box represents the simulation cell. Each cell contains a H_3O^+–HCO_3^- ion pair. Additional species observed are due to visualization with periodic boundary conditions. The vacuum layer is not shown. If the outer layer of the surface is considered as the one composed of the top iodine atoms directly in contact with the vacuum, then the distance between the carbon atom of the bicarbonate and the outer layer amounts to 4.5 Å.

The entire process may be considered as a subsurface-surface reaction which is quite unusual and new for CO_2 chemistry. Note, however, that the active site for bicarbonate formation is just 4.5 Å below the outer surface layer formed by the iodine atoms, see Fig. S13. Indeed, we describe a subsurface reaction and not a bulk or solid state type process.

Generic list of acronyms and abbreviations

AES	Auger electron spectroscopy
AFM	atomic force microscopy
CMA	cylindrical mirror analyzer
CNTs	carbon nanotubes
CVD	chemical vapor deposition
DFT	density functional theory
EBL	electron beam lithography
EDX/EDS	energy dispersive X-ray spectroscopy
GC	gas chromatograph
HDS	hydrodesulphurization
HREELS	high resolution electron energy loss spectroscopy
IF	inorganic fullerene-like nanoparticles
LEED	low energy electron diffraction
MBRS	molecular beam relaxation spectroscopy
MCS	Monte Carlo simulations
NDSU	North Dakota State University
NT	nanotubes
NP	nanoparticles
PNNL	Pacific Northwest National Laboratory
PVD	physical vapor deposition
SEM	scanning electron microscopy
STM	scanning tunneling microscopy
TEM	transmission electron microscopy
TiNTs	TiO_2 nanotubes
TDS	thermal desorption spectroscopy
TOF	time of flight spectroscopy
UHV	ultra-high vacuum
UPS	ultraviolet photoelectron spectroscopy
UV	ultraviolet
XPS	X-ray photoelectron spectroscopy

References

1   *W. Taifan, J. F. Boily and J. Baltrusaitis,* Surface Science Reports, 2016, **71,** 595–671

2   *H. J. Freund and M. W. Roberts,* Surface Science Reports, 1996, **25,** 225

3   *U. Burghaus,* Progress in Surface Science, 2014, **89,** 161

4   *U. Burghaus,* Catal. Today, 2009, **148,** 212-220

5   *U. Burghaus,* chapter 3, in NEW AND FUTURE DEVELOPMENTS IN CATALYSIS: ACTIVIATION OF CARBON DIOXIDE, S.L. Suib (Volume Editor), Publisher Elsevier, 2013, http://dx.doi.org/10.1016/B978-0-44-453882-6.00003-6

6   NEW AND FUTURE DEVELOPMENTS IN CATALYSIS: ACTIVIATION OF CARBON DIOXIDE, S.L. Suib (Volume Editor), Publisher Elsevier, 2013

7   *M. Karplus and R. N. Porter,* 1970, Benjamin/Cummings, ISBN 0-8053-5218-X

8   *R. Hammami, H. Batis and C. Minot,* Surf. Sci., 2009, **603,** 3057-3067

9   *G. Rakotovelo, P. S. Moussounda, M. F. Haroun, P. Légaré, A. Rakotomahevitra, M. Rakotomalala and J. C. Parlebas,* Surface Science, 2009, **603,** 1221–1228

10   *J. Wang and U. Burghaus,* Journal of Chemical Physics, 2005, **122,** 044705-11

11   *E. Kadossov, J. Justin, M. Lu, D. Rosenmann, L. E. Ocola, S. Cabrini and U. Burghaus,* Chem.Phys.Lett., 2009, **483,** 250-253

12   *J. Shan, A. Chakradhar, Z. Yu and U. Burghaus,* Chem. Phys. Lett., 2011, **517,** 46-50

13   *W. Nie, H. Tsai, R. Asadpour, J. C. Blancon, A. J. Neukirch, G. Gupta, J. J. Crochet, M. Chhowalla, S. Tretiak, M. A. Alam, H. L. Wang and A. D. Mohite,* Science, 2015, **347,** 522-525

14   *J. Yang, B. D. Siempelkamp, D. Liu and T. L. Kelly,* ACS nano, 2015, **2,** 1955–1963

15   *G. Kresse and J. Hafner,* Phys. Rev. B, 1993, **47,** 558-561

16   *G. Kresse and J. Hafner,* Phys. Rev. B, 1994, **49,** 14251-14269

17   *G. Kresse and J. Furthmüller,* Phys. Rev. B, 1996, **54,** 11169-11186

18   *G. Kresse and J. Furthmüller,* Comput. Mater. Sci., 1996, **6,** 15-50

19   *P. E. Blöchl,* Phys. Rev. B, 1994, **50,** 17953-17979

20   *J. P. Perdew, J. A. Chevary, S. H. Vosko, K. A. Jackson, M. R. Pederson, D. J. Singh and C. Fiolhais,* Phys. Rev. B, 1992, **46,** 6671-6687

21   *J. P. Perdew, K. Burke and M. Ernzerhof,* Phys. Rev. Lett., 1996, **77,** 3865-3868

22   *J. Even, L. Pedesseau, J.-M. Jancu and C. Katan,* The Journal of Physical Chemistry Letters, 2013, **4,** 2999-3005

23   *U. v. Barth and L. Hedin,* Journal of Physics C: Solid State Physics, 1972, **5,** 1629

24   *G. Scalmani and M. J. Frisch,* Journal of Chemical Theory and Computation, 2012, **8,** 2193-2196

25   *D. Hobbs, G. Kresse and J. Hafner,* Physical Review B, 2000, **62,** 11556-11570

26   *Y. Wang, B. G. Sumpter, J. Huang, H. Zhang, P. Liu, H. Yang and H. Zhao,* The Journal of Physical Chemistry C, 2015, **119,** 1136-1145

27   *T. Baikie, Y. Fang, J. M. Kadro, M. Schreyer, F. Wei, S. G. Mhaisalkar, M. Graetzel and T. J. White,* Journal of Materials Chemistry A, 2013, **1,** 5628-5641

28   *D. Forgacs, M. Sessolo and H. J. Bolink,* J. Mater. Chem. A, 2015, **3,** 14121

29   *A. A. Mamun, T. T. Ava, H. R. Byun, H. J. Jeong, M. S. Jeong, L. Nguyen, C. Gausina and G. Namkoong,* Phys. Chem. Chem. Phys., 2017, **19,** 19487--19495

30   *M. Long, T. Zhang, Y. Chai, C. F. Ng, T. C. W. Mak, J. Xu and K. Yan,* Nature Communications, 2016, **7,** 13503

31   *L. K. Ono, M. R. Leyden, S. Wang and Y. Qi,* Journal of Materials Chemistry A, 2016, **4,** 6693-6713

32   *G. Niu, X. Guo and L. Wang,* J. Mater. Chem. A, 2015, **3,** 8970–8980

33   *C. V. Kumar, G. Sfyri, D. Raptis, E. Stathatos and P. Lianos,* RSC Advances, 2015, **5,** 3786-3791

34   *E. J. Juarez-Perez, Z. Hawash, S. R. Raga, L. K. Ono and Y. Qi,* Energy Environ. Sci., 2016, **9,** 3406--3410

35   *S. Funk, J. Goering and U. Burghaus,* Applied Surface Science, 2008, **254,** 5271-5275

36   *S. Funk, T. Nurkic and U. Burghaus,* Applied Surface Science, 2007, **253,** 4860-4865

37   *P. A. Redhead,* Vacuum, 1962, **12,** 203

38   *K. C. Waugh,* Catal. Today, 1999, **53,** 161